



Variability and evolution of mid-latitude stratospheric aerosol budget from 22 years of ground-based lidar and satellite observations

5 Sergey M. Khaykin¹, Sophie Godin-Beekmann¹, Philippe Keckhut¹, Alain Hauchecorne¹, Julien Jumelet¹, Jean-Paul Vernier^{2,3}, Adam Bourassa⁴, Doug A. Degenstein⁴, Landon A. Rieger⁴, Christine Bingen⁵, Filip Vanhellemont⁵, Charles Robert⁵, Matthew DeLand⁶, Pawan K. Bhartia⁷

10 ¹ LATMOS/IPSL, UVSQ Université Paris-Saclay, UPMC Univ. Paris 06, CNRS, Guyancourt, France.

² Science Systems and Applications, Inc., Hampton, Virginia, US.

³ NASA Langley Research Center, Hampton, Virginia, US.

⁴ Institute of Space and Atmospheric Studies, University of Saskatchewan, Saskatoon, Saskatchewan, Canada.

15 ⁵ Royal Belgian Institute for Space Aeronomy, Brussels, Belgium

⁶ Science Systems and Applications, Inc., Lanham, Maryland, USA,

⁷ NASA Goddard Space Flight Center, Greenbelt, Maryland, USA

20 *Correspondence to:* Sergey M. Khaykin (sergey.khaykin@latmos.ipsl.fr)

Abstract

25 The article presents new high-quality continuous stratospheric aerosol observations spanning 1994-2015 at the French Observatoire de Haute-Provence (OHP, 44 °N, 6 °E) obtained by two independent regularly-maintained lidar systems. Lidar series are compared with global-coverage observations by Stratospheric Aerosol and Gas Experiment (SAGE II), Global Ozone Monitoring by Occultation of Stars (GOMOS), Optical Spectrograph and InfraRed Imaging System (OSIRIS), Cloud-Aerosol Lidar with Orthogonal Polarization (CALIOP) and Ozone Mapping Profiling Suite (OMPS) satellite instruments, altogether covering the time span of OHP lidar measurements.

30 Local OHP and zonal-mean satellite series of stratospheric aerosol optical depth are in excellent agreement, allowing for accurate characterization of stratospheric aerosol evolution and variability at Northern mid-latitudes during the post-Pinatubo era. The combination of local and global observations is used for careful separation between volcanically-perturbed and quiescent periods. While the volcanic signatures dominate the stratospheric aerosol record, the background aerosol abundance is found to be modulated remotely by poleward transport of convectively-cleansed air from the deep tropics and aerosol-laden air from the Asian monsoon region. The annual cycle of background aerosol at mid-latitudes, featuring a minimum during late spring and a maximum during late summer, correlates with that of water vapour from Microwave Limb Sounder (MLS).

35 Observations covering two volcanically-quiescent periods over the last two decades provide indication of a growth in the non-volcanic component of stratospheric aerosol. A statistically-significant factor of two increase of non-volcanic aerosol since 1998, seasonally restricted to late-summer and fall, is associated with the influence of the Asian monsoon and growing pollution therein.

45

50



1 Introduction

55 The role of stratospheric aerosol burden in climate variability and ozone chemistry is well
recognized. Long-term observations of stratospheric aerosol are essential for interpretation of global
atmospheric temperature and ozone layer variability (SPARC, 2006; Solomon et al., 2011). Regular
vertically-resolved observations of stratospheric aerosol began in 1970s, 10 years after the
60 pioneering in situ measurements by Junge et al. (1961) and remote detection by Fiocco and Grams
(1964). Global information on stratospheric aerosol is available since the late 1970s from various
satellite missions, reviewed by SPARC (2006) and Kremser et al. (2016).

Volcanic eruptions with Volcanic Explosivity Index (VEI) ≥ 4 injecting sulphur into the
stratosphere are a major source of stratospheric aerosol. In the absence of strong eruptions, the
permanent stratospheric aerosol layer (also termed background aerosol) is commonly attributed to
65 sulphuric gas precursors such as OCS and SO₂ emitted at the surface and lofted into the stratosphere
by deep convection and the Brewer-Dobson circulation. The removal of aerosols from the
stratosphere occurs mainly by sedimentation and through quasi-isentropic transport of air masses in
tropopause folds (SPARC, 2006).

Long-term evolution of stratospheric aerosol has been a focus of several studies (see review by
70 Kremser et al., 2016 and references therein). Remote and in situ observations between 1970s and
2004 did not reveal any significant change in the background aerosol (Deshler et al., 2006). Several
further studies (Hoffman et al., 2009; Vernier et al., 2011a; Trickl et al., 2013) reported an increase
of stratospheric aerosol levels since 2002, whereas the source of this increase was debated. Initially
this increase was attributed by Hoffman et al. (2009) to a rapid rise of Asian sulfur emissions,
75 uplifted by deep convection within the Asian monsoon. Vernier et al. (2011a) used global satellite
observations to demonstrate that the increase was primarily caused by minor volcanic eruptions,
whose impact should be carefully accounted for when analyzing the change in aerosol load.
Although of much smaller significance compared to Pinatubo or El Chichon, these minor eruptions
had a notable effect on climate (Solomon et al., 2011; Fyfe et al., 2013; Santer et al., 2014; 2015;
80 Andersson et al., 2015), suggesting that even small variability of stratospheric aerosol matters.

It is now widely accepted that volcanic eruptions largely determine the observed variability of
stratospheric aerosol load (Kremser et al., 2016). Meanwhile, recent studies report a measurable
increase of non-volcanic component of aerosol within Asian Tropopause Aerosol Layer (ATAL),
occurring during Northern summer above the Asian monsoon (Vernier et al., 2015; Yu et al., 2015).
85 Accurate long-term measurements are indispensable to quantify the human-induced change in
stratospheric aerosol.

While measurements from space are performed with a large diversity of techniques, long-term
ground-based observations are highly valuable as they ensure the continuity and coherence of
stratospheric aerosol record. During volcanically quiescent conditions accurate detection of
90 stratospheric aerosols becomes challenging as the aerosol scattering signal becomes small compared
to the molecular scattering. In an effort to better characterize the evolution of stratospheric aerosol
load and its variability at Northern mid-latitudes during the post-Pinatubo era we utilize a continuous
22-year observation record from Observatoire de Haute-Provence and a variety of satellite data sets.

The paper is organized as follows: Section 2 provides information on the OHP lidars, aerosol
95 retrieval and satellite data sets exploited. Section 3 compares the OHP lidar and satellite aerosol
records. Section 4 provides examples of volcanic plumes detections and distinguishes volcanically-
perturbed and quiescent periods. Section 5 describes the variability, annual cycle and long-term
change of background aerosol. Section 6 discusses the proposed interpretation and concludes the
100 paper.

2 Instruments and data sets

2.1 Observatoire de Haute-Provence lidars



105 The Observatoire de Haute-Provence (OHP) located in Southern France (43.9° N, 5.7° E, 670 a.s.l.) is one of the Alpine stations within the Network for Detection of Atmospheric Composition Change (NDACC). The site is characterized by a high rate of clear nights and offers an opportunity for frequent lidar observations.

For over three decades two independent lidar systems have been operated at OHP station: a Differential Absorption Lidar (DIAL) for stratospheric ozone (hereafter referred to as LiO3S) and a Rayleigh-Mie-Raman lidar for middle atmosphere temperature measurements (hereafter referred to as LTA). Both LiO3S (Godin-Beekmann et al., 2003) and LTA (Hauchecorne et al., 1992) lidar systems provide routine measurements since 1985 and 1979 respectively. After a technical upgrade of both lidars in 1994 the mean measurement rate is 10-12 acquisition nights per month.

110 While LTA system includes a separate telescope and detection channel for clouds and aerosol (Chazette et al., 1995; Keckhut et al., 2005; Hoareau et al., 2013), this study exploits the primary, more powerful detection channel of LTA (532 nm) instrument, restricted to altitudes above 12-13 km due to saturation of detectors by strong Rayleigh returns below.

115 The off-line channel of LiO3S lidar features Nd:YAG laser frequency-tripled to 355 nm, which operates at 50 Hz pulse rate and 42 mJ/pulse energy. The total collective surface of its mosaic 4-mirror telescope is 0.88 m². The primary low gain channel of LTA makes use of a frequency-doubled Nd:YAG laser emitting at 532 nm with a pulse rate of 50 Hz and 350 mJ/pulse energy and a 0.03 m² telescope. The maximum vertical resolution for both lidars amounts to 15 m, however the vertical profiles are usually reported at 150 m resolution.

125 2.2 Lidar aerosol retrieval

For retrieving vertical profiles of stratospheric aerosol we use LiO3S and LTA measurements spanning 1994 through 2015 with a total number of 3118 (LiO3S) and 2691 (LTA) nights of lidar acquisitions, lasting 3-5 hours each. The retrieval is based on the Fernald-Klett inversion method (Fernald, 1984; Klett, 1985), which provides backscatter and extinction coefficients. The scattering ratio (SR) is computed as a ratio of total (molecular plus aerosol backscattering) to molecular backscattering. The reference zero-aerosol altitude is set between 30 and 33 km. LiO3S 355 nm data are converted to 532 nm using wavelength exponents for particle extinction (κ_e) and backscatter (κ_b) adapted from Jäger and Deshler (2002; 2003) and set to $\kappa_e=1.6$ and $\kappa_b=1.3$ after the year 1997. Similarly, the extinction-to-backscatter (lidar) ratio is set to 50 sr after 1997, which is a commonly assumed value for volcanically-quiescent conditions and periods of moderate eruptions (e.g. Trickl et al., 2013; Ridley et al., 2014; Sakai et al., 2016). The molecular backscatter is calculated from National Centers for Environmental Prediction (NCEP) daily meteorological data interpolated to OHP location. The lidar raw signals have been subjected to a thorough quality screening, accounting for the instruments' technical health log. The overall rejection rate amounted to 17% and 11% for LiO3S and LTA respectively.

135 Cumulative uncertainties of the backscatter measurements induced by random detection processes, possible presence of aerosol at the reference altitude and the error in lidar ratio value do not exceed 7% as reported by Chazette et al., (1995). Another major source of uncertainty is the molecular number density derived from atmospheric pressure and temperature. The lidar inversion is particularly sensitive to the molecular density at the reference altitude, where the lidar return is assumed to be purely due to molecular scattering. Since the routine radiosonde measurements, commonly used to derive the molecular density, rarely reach the reference altitudes above 30 km, reanalysis data are required for the inversion.

145 We compared the monthly-mean series of integrated backscatter coefficient in 17 - 30 km layer retrieved using NCEP and ERA-Interim reanalyses and found a mean relative difference of 5.6 % between both datasets. This value may serve as an estimate for the uncertainty due to molecular density. As a result, the total uncertainty of individual backscatter measurement is below 10 %. We note that the uncertainty in the assumed lidar ratio has a very limited effect on the derived values of backscatter coefficient and scattering ratio (~ 0.15 %/sr). At the same time, error in lidar ratio affects



155 proportionally the aerosol extinction and optical depth, whose uncertainty may thus be somewhat
larger.

2.3 Satellite aerosol sounders

160 SAGE II (Stratospheric Aerosol and Gas Experiment) (Russel and McCormick, 1989) is a
seven-channel Sun photometer. It was launched onboard the Earth Radiation Budget Satellite in 1984
and provided solar occultation measurements of stratospheric aerosol extinction with a vertical
resolution of 1 km until mid-2005. SAGE II fully covers the latitude range from 80° S to 80° N in 1
(2) month with a typical rate of 32 measurements per day (reduced to 16 after 2000). We used SAGE
165 II version 7.0 aerosol extinction data at 525 nm converted to 532 nm using a wavelength exponent
 $\kappa=1.6$.

GOMOS (Global Ozone Monitoring by Occultation of Stars) (Bertaux et al., 2010), is a
UV/Visible/NIR spectrometer launched in 2002 onboard ENVISAT and operating until April 2012.
The instrument performed occultations of selected stars by means of four spectrometers. We use
170 aerosol extinction profiles retrieved by the AerGOM algorithm which was developed using an
improved aerosol parameterization (Vanhellemont et al., 2016)

OSIRIS (Optical Spectrograph and InfraRed Imaging System) is a limb scatter instrument
launched onboard the Odin satellite in 2001 and providing measurements of various chemical species
and aerosol extinctions (McLinden et al., 2012). The primary instrument is Optical Spectrograph
175 (OS) operating in 284-810 nm range and providing between 100 and 400 occultations per day
depending on the time of year. The principle of limb scattering and the Odin satellite orbit limit the
coverage in the winter hemisphere in such a way that no data are available above 45° N during 2-
month period around the winter solstice. We use OSIRIS version 5.07 stratospheric aerosol
extinction data at 750 nm (Bourassa et al., 2012) converted to 532 nm using $\kappa=2.0$.

180 CALIOP (Cloud-Aerosol Lidar with Orthogonal Polarization) onboard CALIPSO satellite
platform is a nadir-viewing active sounder (Winker et al., 2010). Operational since June 2006,
CALIOP provides range-resolved measurements of elastic backscatter at 532 nm and 1064 nm with a
vertical resolution of around 200 m in the stratosphere. CALIOP lidar makes use of a Nd:Yag laser
operating at 20.2 Hz with a 110 mJ/pulse power and a 0.78 m² telescope. The data used here are
185 based on night-time 532 nm level 1B version 4.00 product, post-processed using a treatment
described by Vernier et al. (2009). The backscatter data are converted to extinction using lidar ratio
of 50 sr and data are cloud-cleared in the upper troposphere using a depolarization ratio threshold of
5%.

OMPS (Ozone Mapping Profiling Suite) LP (Limb Profiler) onboard NPP/Suomi satellite,
190 launched in 2012 measures limb-scattered light with a sampling rate of up to 7000 measurements per
day (Jaross et al., 2014). Regular observations of aerosol extinction are available since April 2012.
We use V0.5 extinction data at 675 nm (DeLand et al., 2016) converted to 532 nm using $\kappa=1.8$.

3 Intercomparison of OHP lidars and satellites sounders

195 Figure 1 shows time series of monthly-averaged stratospheric Aerosol Optical Depth between
17 and 30 km altitude ($sAOD_{1730}$) derived from OHP lidars and satellite data sets. The choice of the
lower integration boundary is explained hereinafter. Monthly-mean values comprise on average of 9
(LiO3S) and 11 (LTA) individual acquisition nights (after quality screening), whereas the satellite
200 zonally- and monthly-averaged values contain 72 (SAGE II), 128 (GOMOS), 97 (OSIRIS), $\sim 4 \cdot 10^6$
(CALIOP) and $\sim 3 \cdot 10^3$ (OMPS) individual measurements. The average standard deviation for
monthly averages of OHP lidars' $sAOD_{1730}$ amounts to 10.4 % (LiO3S) and 7.8% (LTA). The
agreement between all data sets is remarkable despite the large variety of measurement techniques.
The results of intercomparison are summarized in Tab. 1.

205 The OHP lidars agree to within $0.7 \pm 2.4\%$ (mean relative difference and two Standard Errors,
2 SE) with a correlation coefficient of 0.9. The LiO3S and LTA lidars compared to the satellite mean



210 sAOD₁₇₃₀ show a difference of $-1.5 \pm 2.2\%$ (2SE) and $-2.7 \pm 2.1\%$ (2 SE) respectively with a correlation of 0.94 for both lidars. The satellite-to-satellite intercomparison shows mean discrepancies below 9% and correlation above 0.8 for any satellite pair except OMPS, whose observation record length is less than 4 years and covers a period with small geophysical variability. Note that the discrepancies may be partly caused by the error in the assumed wavelength exponents and lidar ratio. Indeed, the largest lidar-satellite discrepancies are obtained for the satellite sounders operating at higher wavelengths, i.e. OSIRIS (750 nm) and OMPS (675 nm), whereas the best agreement is between OHP LTA lidar and CALIOP, both operating at 532 nm.

215 Overall, all the biases are well below the statistical errors, which confirms the coherence between the continuous OHP record and the combined satellite time series. Note that the satellite series are zonally averaged over 10° latitude belt centred at OHP latitude in order to increase the sampling. The coherence between lidar and satellite series suggests that the stratospheric aerosol burden is zonally-uniform at least on a monthly-mean scale. This may be explained by the presence
220 of strong zonal winds in the stratosphere, which rapidly homogenize the aerosol and tracers in the zonal direction.

The layer between 17 and 30 km, for which the comparison is reported in Fig. 1 and Tab. 1 does not represent the total stratospheric aerosol column. A significant fraction of stratospheric aerosol resides below 17 km (Rideley et al., 2014; Andersson et al., 2015), however an accurate
225 detection of the aerosol abundance in the lowermost stratosphere is more challenging for limb-viewing satellite instruments (Bourassa et al., 2010; Thomason and Vernier, 2013), which may lead to larger discrepancies in sAOD.

Figure 2 displays a comparison of aerosol extinction profiles averaged over two 20-month volcanically-quiet periods 2002-2003 and 2013-2014 covered by time-overlapping
230 observations by two different triplets of satellite sounders. The comparison reveals close agreement between all data sets in the 17-25 km layer whereas above 25 km the lidar profiles show some negative bias compared to satellites, which is most likely related to an error in lidar calibration, relying on the assumption of the absence of aerosol above 30 km, which – as suggested by CALIOP data calibrated at higher altitudes - may not always be the case.

235 Below 17 km the extinction profiles diverge and both OHP lidars show higher values compared to satellite ones. This discrepancy may be due to the use of fixed lidar ratio and wavelength exponents, which may vary with height depending on the size distribution of aerosol. Particularly, the lower stratospheric layers are expected to contain larger particles, accumulating after sedimentation from the higher stratospheric levels (SPARC, 2006). Throughout the paper we
240 restrict to aerosol measurements above 15 km because the lower layer may be contaminated by cirrus clouds, which according to Goldfarb et al. (2001) and Hoareau et al. (2013) may encounter at altitudes up to 14 km above OHP. In addition, measurements by LTA system (optimized for the middle atmosphere) may be affected by incomplete desaturation of the strong lidar returns from lower layers.

245

4 Detection of volcanic plumes and quiescent periods

The remarkable coherence between the lidar- and satellite-based sAOD₁₇₃₀ series demonstrated in the previous section allows for a synergetic use of local and global observations to characterize at
250 best the variability of stratospheric aerosol. Fig. 3 shows sAOD₁₇₃₀ series computed by averaging the OHP lidars and all five satellites data sets. The timing of VEI=4 volcanic eruptions North of 20° S is indicated by vertical arrows, whereas the periods affected by these eruptions are marked by light blue shading (selection criteria are described hereinafter).

Quiescent period 1997 - 2003

255 The sAOD₁₇₃₀ series since 1994 shows a tail of Pinatubo aerosol followed by a stabilisation at a quasi-constant level around mid 1997 according to SAGE II and OHP lidars observations. Between mid-1997 and late 2001 aerosol loading remains stable with no discernible eruption-induced enhancements at Northern Hemisphere (NH) mid-latitudes. This is fully consistent with other mid-



260 latitude lidar observations (Deshler et al., 2006; Trickl et al., 2013). Although some VEI 4 eruptions between 2000 and 2003 have occurred over that time, they had very limited stratospheric impact (Vernier et al., 2011a; Kremser et al., 2016).

265 Importantly, the stratospheric aerosol levels during 1997-2003 period are at or below any previous background period since 1970 (Jäger, 2005; Deshler et al., 2006) and may thus be regarded as a reference level for background stratospheric aerosol, against which further changes in aerosol load should be compared. Both SAGE II and OHP lidars report an average background sAOD_{1730} for the “reference” quiescent period of $2.3 \cdot 10^{-3} \pm 2.4\%$ (2 SE), which is marked in Fig. 3 by dashed line and grey shading, indicating 1- σ range of values.

Volcanically-active period 2003-2013

270 The continuous quiescent period is terminated in late 2003, when the plume of tropical Ruang and Reventador eruptions (Thomason et al., 2008) reaches NH mid-latitudes. The subsequent VEI=4 eruptions of Manam volcano at 4° S (Vanhellemont et al., 2010), Soufriere Hills at 16° N (Prata et al., 2007) and Tavurvur at 4° S lead to step-like increases of sAOD_{1730} . In Summer 2008, two neighbouring VEI 4 eruptions of Okmok and Kasatochi volcanoes at 55° N (Bourassa et al., 2010)
275 result in a rapid increase of sAOD_{1730} followed by a relaxation to quasi-background level with e-folding time of 6 months. In June 2009, the eruption of Sarychev at 48° N (Haywood et al., 2010) increases sAOD_{1730} to $8 \cdot 10^{-3}$, the highest value since 1994. The post-Sarychev recovery is relatively fast, with only 4-5 months of e-folding period, after which sAOD_{1730} returns to background level in January-February 2010.

280 A strong enhancement of sAOD_{1730} follows the eruption of Nabro volcano (14° N) in June 2011. A rapid hemisphere-wide dispersion of Nabro plume was facilitated by the Asian monsoon (Bourassa et al., 2012; Fairlie et al., 2014), although the role of the monsoon in providing an alternative pathway for aerosol and/or SO_2 into the stratosphere is debated (Vernier et al. 2013). Interestingly, the mid-latitude Sarychev eruption and the tropical Nabro eruption resulted in
285 sAOD_{1730} enhancement of nearly the same amplitude, however the removal of Nabro aerosol took much longer time (e-folding period of up to 19 months) according to zonal-mean series derived from CALIOP and OSIRIS.

A better insight into the temporal evolution and vertical structure of Sarychev and Nabro plumes is provided by Fig. 4, showing scattering ratio (SR) profiles obtained by OHP LiO3S lidar during the corresponding volcanic periods. The Sarychev plume was detected at OHP already 10 days after the eruption as sharp SR enhancements below 19 km reaching 3.4 units. A remarkable scatter between the individual profiles points to a rapid three-dimensional evolution of the plume, dispersed by the stratospheric mean zonal flow, which reversed over the course of the plume permanence.

295 The first signatures of Nabro plume were detected at OHP 45 days after the start of eruption. In contrast to the highly variable Sarychev plume, the SR profiles bearing Nabro signature are characterized by a smooth broad-range enhancement reaching 1.7 and relatively small scatter between the individual profiles, suggesting that the plume has already been mixed with the ambient air before arriving at OHP latitude. Noteworthy, the period-averaged SR profiles (black circles in Fig. 4) corresponding to Sarychev and Nabro plumes are of comparable shape and enhancement
300 amplitude.

Post-Nabro period

305 By early-mid 2013 all data sets report sAOD_{1730} stabilizing around $2.7 \cdot 10^{-3} \pm 3.9\%$ (mean lidars) and $3.0 \cdot 10^{-3} \pm 3.5\%$ (mean satellites) and remaining at that level for almost 2 years, through December 2014. In January 2015, the plume of Kelud eruption (Kristiansen et al., 2015) reached OHP latitude as inferred from CALIOP sAOD_{1730} time-latitude section (not shown). The signatures of Kelud plume were observed at OHP until April 2015, after which sAOD_{1730} returns to near background levels. The eruption of Calbuco volcano at 41° S (Romero et al., 2016) in spring 2015 has led to a notable increase of stratospheric aerosol load, as suggested by CALIOP (Fig. 6) and
310 OMPS (not shown) observations, which however provide no indications for the transport of Calbuco



plume to OHP latitude in 2015. Initial analysis of the more recent OMPS data by does not indicate significant transport of the Calbuco plume into the Northern Hemisphere through July 2016 (G. Taha, personal communication).

315 4.1 Selection of volcanically-perturbed periods

Since 1994 the major perturbations of NH stratospheric aerosol load were caused by mid-latitude volcanic eruptions of Okmok/Kasatochi and Sarychev as well as the tropical eruption of Nabro, all readily reflected in OHP lidars and satellite sAOD₁₇₃₀ series (Fig. 1 and 3). The plumes of more distant (tropical) eruptions are not always obvious in sAOD series. In order to accurately distinguish between volcanically-perturbed and quiescent periods we use global-coverage satellite observations to track the spatiotemporal evolution of each volcanic plume. The plumes were detected by examining time-latitude sections of partial sAOD from all satellite records (example for CALIOP is provided in Fig. 6). If a plume was found to extend beyond the tropical belt towards the Northern extra-tropics, the temporal extent of the corresponding volcanic period was determined by comparing the OHP lidar monthly-mean sAOD₁₇₃₀ values and SR profiles obtained after an eruption against those averaged over the “reference” quiescent period 1997-2003. In this way, a period is considered as volcanically-perturbed if both of the following two conditions are fulfilled:

320 i) monthly-mean sAOD₁₇₃₀ value exceeds the 1- σ range of the “reference” quiescent period of 1997-2003 (grey band in Fig. 3);

325 ii) monthly-mean SR profile exceeds the 1- σ range of the “background” SR profile - an average over the entire “reference” quiescent period (grey-filled in Fig.5) in a layer > 2 km thick.

Figure 5 shows the difference between averaged SR profiles for the quiescent and volcanically-perturbed periods in order to clarify the application of the second selection criterion. The black solid curve and grey shading represent the mean SR profile for the “reference” period (1997-2003) and its 1- σ range respectively. The coloured curves show SR profiles corresponding to the aged plumes of tropical eruptions of Ruang, Nabro and Kelud. The maximum SR values of these profiles are remarkably smaller than those observed in a young plume (Fig. 4), however they are visibly beyond the grey-shaded background range of SR. The same consideration holds for the corresponding sAOD₁₇₃₀ values in Fig. 3. This allows for classifying the respective periods as volcanically-perturbed. The timing of VEI 4 eruptions and the lifetime of their plumes as detected at OHP are listed in Tab. 2.

We noted that the time required for a plume to propagate to OHP latitude depends on the eruption season and injection altitude. In particular, the tropical eruptions injecting material directly into the lower stratosphere (e.g. Soufriere Hills or Kelud) would have a longer lifetime in the stratosphere, however their poleward propagation is inhibited during Boreal summer, when stratospheric meridional exchange weakens. For this reason, the Kelud plume has reached OHP latitude only about 10 months after the eruption. The period between the full decay of Nabro plume in early 2013 and the arrival of the aged Kelud plume in late 2014 is characterized by an SR profile (dashed curve in Fig. 5) lying within the background range of values. The sAOD₁₇₃₀ is relatively stable and remains within the background range during this period, which is therefore classified as quiescent.

Another example is the eruption of Merapi (7° S), which occurred in October 2010, shortly before the start of the NH winter season, characterized by enhanced poleward transport into the winter hemisphere. According to CALIOP observations (Fig. 6), the plume of Merapi was transported to OHP latitude in about 2 months, whereas its permanence at NH mid-latitude was limited to 3 months.

360 5 Non-volcanic drivers of aerosol variability

Figure 6 displays the time-latitude section of zonal-mean AOD in a layer between 15 and 19 km (sAOD₁₅₁₉) from CALIOP data and time series of the same quantity obtained by OHP LiO3S



lidar. The 15-19 km layer is chosen because it is directly impacted by most of VEI 4 eruptions and is characterized by efficient quasi-isentropic exchange within the UT/LS (e.g. Kremser et al., 2016).
365 The enhanced poleward transport into the winter hemisphere is exhibited by meridional wind vectors in Fig. 6.

Beside the volcanic plumes, CALIOP observations reveal systematic enhancement in $sAOD_{1519}$ between about 15° and 45° N during the Northern summer, most prominent ones occurring in 2007, 2010, 2013 and 2015. Given its timing and location, this feature can be attributed
370 to the so called Asian Tropopause Aerosol Layer (ATAL) (Vernier et al., 2011b; Thomason and Vernier 2013), occurring in the 15-18 km layer above the Asian summer monsoon and extending to mid-latitudes (Vernier et al., 2015).

Another feature revealed by CALIOP is systematic aerosol depletion in January-February around the equator and spreading poleward. The tongues of aerosol-poor air are readily discernible in
375 2007, 2008, 2010, 2012 and 2015 whereas in the other years they are scrambled by volcanic plumes or hardly discernible from the low background aerosol burden. The timescale of poleward transport of clean air can be inferred from the shape of the clean air tongues – fast within the tropical belt and slower across the subtropical stratospheric barrier. The systematic aerosol depletion in the TTL during Austral summer was attributed by Vernier et al. (2011c) to fast convective cross-tropopause
380 transport (overshooting) of clean tropospheric air (cleansing). The clean air reaches OHP latitude in about 3 months, which is reflected in the OHP lidar series, showing a recurring minimum in late spring - early summer.

The time-latitude pattern of $sAOD_{1519}$ can be paralleled with that of water vapour at 100 hPa level from Aura Microwave Limb Spectrometer (MLS) (Waters et al., 2006) version 4.2 data
385 (Livesey et al., 2015). Dashed and dotted contours in Fig. 6 encircle the areas of water vapour mixing ratio of 3, 4 and 5 ppmv. The 5 ppmv (red dashed) contour shows the area of annual maximum of water, emerging during the Northern summer, which can be attributed to the moisture flux from the Asian monsoon (Park et al., 2007; Schwartz et al., 2015). The moist air is traceable to OHP latitude and coincides in time and space with the annual maximum of $sAOD_{1519}$, associated
390 with ATAL. Spatiotemporal match of the aerosol and water vapour annual maxima suggests the same origin of the both – the Asian monsoon.

The areas of annual minimum of water vapour (black dashed contours) correlate with the minima in TTL aerosol load, both occurring during the Southern summer. While the annual minimum of water vapour can be readily explained by the coldest TTL temperatures in January-February leading to enhanced dehydration of the TTL (e.g. Holton et al., 1995), the aerosol reduction
395 can be attributed to convective cleansing during Austral summer (Vernier et al., 2011c). Both dry and clean air features show similar poleward propagation. Overall, the seasonal cycle of stratospheric aerosol loading in the TTL, featuring a maximum in NH during Boreal summer and minimum around the equator during Austral summer is similar to that of water vapour.

400

5.1 Annual cycle

Fig. 7a shows climatological annual cycle of scattering ratio (SR) profile from OHP LiO3S lidar based on the selected periods considered as volcanically-quiet (see Fig. 3). Throughout the
405 seasons and altitude layers the SR does not exceed 1.08, meaning that for the quiet conditions the aerosol backscatter constitutes less than 8% of the molecular backscatter. The permanent layer of aerosol in the stratosphere, also referred to as Junge layer (Junge et al., 1961), is commonly attributed to sulphuric acid precursors emitted at the surface and eventually transformed into H₂SO₄-H₂O liquid aerosol mixture (e.g. Brock et al., 1995).

The amplitude of annual cycle of background aerosol is small but variable with altitude. The upper boundary of Junge layer peaks in winter, which is likely related to a weaker transport barrier between the tropical aerosol reservoir and mid-latitude stratospheric overworld during Northern winter, when the wave induced meridional mixing in NH is most pronounced (Holton et al., 1990; Hitchman et al., 1994). Note that the meridional divergence of tropical air in the stratosphere is also
410



415 modulated by the QBO, where the westerly shear phase favours the poleward transport during northern winter (Trepte and Hitchman, 1992).

In the middle layer (19-25 km), the SR varies between 1.04 and 1.07 and shows a smooth maximum in Spring. The lowermost layer, below 19 km exhibits a more pronounced annual cycle, featuring a minimum in May at 16 km, which propagates to 17 km by the end of August. In view of its altitude range and timing, this minimum can be attributed to advection of convectively-cleansed
420 air from the TTL after the Austral summer convective season (Vernier et al., 2011c) and reaching mid-latitudes in about 3 months as was concluded from Fig. 6. The late spring minimum appears to be a robust feature captured by all other satellites (not shown), independently of the observation period. Starting from August, the clean air in the LS is progressively replaced by aerosol-enriched air,
425 presumably originating from the ATAL. Note that the initial inference on the extension of ATAL to OHP latitude is made on the base of CALIOP time-latitude section in Fig. 6. The SR between 15 and 16 km reaches a maximum in October and reduces gradually over the course of the winter. Importantly, for any quiescent subperiod over the course of 22 yr OHP series, the pattern is essentially the same.

430 Fig 7b provides a satellite zonal-mean view on the non-volcanic aerosol annual cycle observed by CALIOP since 2006. The month-altitude pattern of zonal-mean background aerosol revealed by CALIOP is fairly similar to that obtained by OHP lidar. The main features, namely the winter maximum of the Junge layer upper boundary, the spring maximum of SR in the middle layer (19-25 km) and the upward propagation of the late-spring clean feature are readily discernible in both OHP
435 and CALIOP climatologies. Whereas the general patterns appear similar, comparison of the SR vertical distribution reveals some discrepancies between the OHP lidar and CALIOP, with the latter showing slightly higher (lower) SR values in the uppermost (lowermost) layer. The same conclusion was drawn from the comparison of extinction profiles in Fig. 2 (see Sect. 3 for interpretation of the discrepancies). In addition, the maximum of SR in autumn at 15-16 km, attributed to ATAL, is less
440 pronounced in CALIOP section, which is likely due to zonal averaging, reducing the meridionally-restricted ATAL signal (Fig. 2 in Vernier et al., 2015).

In the previous section we noted a relation between time-latitude variation of aerosol and water vapour in the lower stratosphere. Fig. 7c provides further evidence to this finding. Similarly to
445 aerosol, the LS water vapor annual cycle exhibits the upward propagation of the late-spring minimum, followed by the maximum in autumn. As already pointed out on the base of Fig. 6, both aerosol and water vapour in the mid-latitude LS are modulated by poleward transport of clean (dry) air from the deep tropics and aerosol-rich (wet) air from the Asian monsoon region. In fact, the annual cycle the extra-tropical water vapour bears an imprint of the tropical H₂O “tape recorder” (Mote et al., 1996) lagged by the timescale of poleward transport from the TTL (e.g. Hoor et al.,
450 2010). The same applies effectively to background aerosol, leading to similar month-altitude patterns of aerosol and water, as Fig. 7 suggests.

5.2 Long-term change in stratospheric aerosol burden

455 Detection of long-term change in non-volcanic component of stratospheric aerosol is complicated by frequent minor eruptions of stratovolcanoes, whose plumes may persist in the stratosphere for several years, whilst decaying exponentially. A thorough analysis of the trends in the background stratospheric aerosol over 1971-2004 period (covering 3 quiescent periods) was carried out by Deshler et al. (2006), who concluded on the absence of long-term change. The 22-year
460 stratospheric aerosol series provided here covers two quiescent periods: the “reference” six-year long period 1997-2003 and a recent post-Nabro two-year long period 2013-2014. This new-era quiescent period is characterized by stabilization of stratospheric aerosol load at near-background level, rendering it suitable for comparison against the “reference” quiescent period. In this way, a positive change of $13.9 \pm 4.5\%$ (2SE) can be inferred by comparing average sAOD₁₇₃₀ values over the two
465 periods. This estimate may be considered as an upper limit of the trend in non-volcanic aerosol the NH mid-latitude stratosphere, however not without caution. First, it is the limited time span of the



new quiescent period, three times shorter than the “reference” one. Second, a possible influence of eruptions with $VIE=3$, which may occasionally penetrate into the stratosphere (Carn et al., 2015; Mills et al., 2016). The second, however, may as well be true (although not detected or reported) for the “reference” quiescent period. Furthermore, the observations exploited here provide no indication of the influence of eruptions other than those listed above (Tab. 2).

If the change in stratospheric aerosol load is largely due to non-volcanic processes, then the most likely source is the growing Asian emissions of aerosol precursors (Smith et al., 2011), transported into the lower stratosphere by the Asian monsoon (Randel et al., 2010). Indeed, the AOD of ATAL over Eastern Mediterranean, downwind of South-East Asia (Lawrence and Lelieveld, 2010), has increased three times since the late 1990s as inferred from SAGE II and CALIOP observations by Vernier et al. (2015). OHP site is influenced by the Asian anticyclone and its composition, as shown above, hence the change in ATAL AOD is expected to be reflected in OHP long-term series. However, given that the manifestation of ATAL signal in OHP observations is limited to autumn season and lower stratosphere, the change in non-volcanic aerosol should be evaluated with respect to the season and the layer.

Fig. 8a displays vertically and seasonally resolved change in non-volcanic sAOD over 18 years. The statistically significant increase by a factor of two in LS is restricted to late summer and early fall, i.e. in phase with the Asian monsoon signatures detected in aerosol and water vapor. Note that little or no (statistically significant) increase is observed in other seasons, which suggests that accumulation of volcanic aerosols (if any) is unlikely to be the reason for the positive trend. Indeed, zero change in the LS during late spring, i.e. when the tropical air reaches NH mid-latitudes, rules out the effect of unaccounted tropical plumes on the trend estimates.

Further insight into the long-term change of background aerosol is provided in Fig 8b, showing the evolution of AOD in September within the altitude layer characterized by the maximum growth of AOD. Both OHP lidar and satellites provide a clear indication of the increase of AOD with time. The value in 2010, representing the post-Sarychev quiescent period, is slightly higher than the post-Nabro values, however its contribution to the linear regression is limited to 12 %. The linear regression essentially rests upon the two quiescent periods separated in time: 1998 – 2004 and 2013 – 2015, hence the trend value largely depends on the quantification of the aerosol level during the second period. This post-Nabro quiescent period was interrupted by the arrival of Kelud plume at OHP latitude in early 2015. By September 2015 the Kelud plume is no longer observed at OHP: the value in September 2015 is not much different from the pre-Kelud observations in 2013 and 2014, which suggests that the trend estimate is unaffected by the Kelud plume. Lidar observations at Tsukuba, 36° N (Sakai et al., 2016) do not show indication of the presence of Kelud plume in 2015.

6 Discussion and summary

Over the last two decades NH stratosphere was perturbed by a series of minor volcanic eruptions, leaving strong but transient signals in stratospheric aerosol load. A combination of concurrent local and global observations was used to carefully separate between volcanically-perturbed and quiescent periods. The volcanic plumes and their meridional dispersion were detected using satellite observations, whereas determination of a plume’s lifetime was done by comparing OHP lidar measurements against the “reference” levels of background aerosol, corresponding to 1997-2003 period. This approach suffers from the limited sensitivity of remote sensing techniques to low aerosol concentrations, however it is the best that can be provided using the available observations.

The selection of quiescent periods is particularly challenging during 2003-2012 period, characterized by frequent minor eruptions, occurring sometimes before the previous plume has fully decayed. However, the criteria applied allow identifying several brief sub-periods over 2003-2012, during which the stratospheric aerosol attains background levels. The quiescent periods, constituting



520 a considerable fraction (57%) of the 22-year span of OHP observations, yield a wealth of data for establishing a robust climatology of background aerosol at northern mid-latitudes.

Analysis of non-volcanic fraction of data suggests that the annual cycle of mid-latitude background stratospheric aerosol is largely driven by remote (tropical) processes: convective cross-tropopause transport of *clean* air (Vernier et al., 2011c) during southern summer and *polluted* air from the Asian monsoon (Randel et al, 2010; Vernier et al. 2015; Yu et al., 2015) during northern summer, both followed by poleward transport. Although this interpretation is rather robust, alternative contributors should also be considered.

Alternatively, the late-spring minimum in the lower stratosphere might be attributed to release of clean air from within the Arctic vortex after its breakup or gravitational settling of larger particles and their sink through the tropopause folds (SPARC, 2006). However the time-latitude variation of aerosol and water vapour unequivocally point to the poleward transport, thereby providing no support to these hypotheses. The clean air obviously originates from the TTL and whatever mechanisms are responsible (injections into the stratosphere or scavenging in tropopause clouds), the TTL cleansing is an important driver of the annual cycle of stratospheric aerosol at global scale. It also appears that the cleansing process not only modulates the background aerosol but limits the lifetime of weak plumes residing mainly in the lower stratosphere.

535 The late-summer aerosol maximum might partly be due to mid-latitude summertime forest fires and pyroconvection, whose stratospheric impact is recognized (Fromm et al., 2008; 2010). However these events are rare and thus unlikely to contribute significantly to the multi-year averages. The coincidence between water vapor and non-volcanic aerosol annual maxima in the NH midlatitude LS suggests that these air masses originate from the Asian monsoon, whose influence on the extratropical LS in late summer and early fall is well known (Vogel et al., 2014; Müller et al., 2016). Indeed, according to trajectory analyses by Garny and Randel (2016), 15% of the diabatic trajectories released at 360 K within the Asian anticyclone travel to the extratropical LS in 30 days or more, which is consistent with 1-2 months lag of the aerosol and water vapour maxima with respect to the Asian monsoon season.

545 The influence of Asian monsoon on the composition of lower stratosphere at OHP – as suggested by our analysis – implies that the increase in ATAL AOD reported by Vernier et al. (2015) and Yu et al. (2015) should also be reflected in OHP lidar observations. Indeed, after removal of volcanically-perturbed data we observe a doubling of LS partial AOD since 1998 in late summer and early fall, i.e. in phase with the ATAL signal detected at OHP.

550 Our trend estimate is consistent with that of Vernier et al (2015), who found a tripling of aerosol extinction anomaly (summer-to-winter ratio) above the Eastern Mediterranean. As it appears, the analysis of long-term change in non-volcanic aerosol with respect to the season and altitude layer is the only way to obtain a credible trend estimate, in which the effect of unaccounted volcanic plumes is minimized. In this way, the post-Nabro quiescent period, largely determining the observed trend, provides an accurate reference for assessment of long-term change in non-volcanic aerosol load.

560 The annual cycle of background aerosol is shown to reflect the meridional exchange processes, whereas its long-term evolution points to increasing anthropogenic contribution to stratospheric aerosol budget. This effect appears very small compared to volcanic influence, however it should not be ignored. Long-term continuous observations of stratospheric aerosol available from NDACC lidar network are indispensable to follow the evolution of stratospheric aerosol and detect its human-induced change.

565 Acknowledgements

All data sets and codes used to produce this study can be obtained by contacting Sergey Khaykin (sergey.khaykin@latmos.ipsl.fr). The GOMOS AerGOM data can be obtained by contacting Christine Bingen (Christine.Bingen@aeronomie.be). We thank the personnel of OHP for conducting lidar measurements. The work was done with the support of French Institut National des Sciences de l'Univers (INSU) of the Centre National de la Recherche Scientifique (CNRS) and of

570



Centre National d'Etudes Spatiales (CNES). We thank Laurent Blanot (Acri ST) and Nickolay Kadyrov (IPSL) for their help with satellite data handling. OMPS LP Version 0.5 aerosol extinction coefficient data are produced by the LP processing team (<https://ozoneaq.gsfc.nasa.gov/data/omps/>). The AerGom project was financed by the European Space Agency (contract number 22022/OP/I-OL). Charles Robert's research was supported by a Marie Curie Career Integration Grant within the 7th European Community Framework Programme under grant agreement n°293560, the European Space Agency within the Aerosol_CCI project of the Climate Change Initiative and the Belgian Space Science Office (BELSPO) through the Chercheur Supplémentaire programme. The following satellite data used in this study are publically available: CALIPSO, https://eosweb.larc.nasa.gov/project/calipso/calipso_table; SAGE II, https://eosweb.larc.nasa.gov/project/sage2/sage2_table; OSIRIS, <http://odin-osiris.usask.ca/>; MLS, http://mls.jpl.nasa.gov/products/h2o_product.php.

585

References

- Andersson, S., Martinsson, B., Vernier, J.-P., Friberg, J., Brenninkmeijer, C., Hermann, M., Velthoven, M., and Zahn, A.: Significant radiative impact of volcanic aerosol in the lowermost stratosphere, *Nat. Commun.*, 6, 7692, doi:10.1038/ncomms8692, 2015.
- Bertaux, J. L., Kyrölä, E., Fussen, D., Hauchecorne, A., Dalaudier, F., Sofieva, V., Tamminen, J., Vanhellemont, F., Fanton d'Andon, O., Barrot, G., Mangin, A., Blanot, L., Lebrun, J. C., Pérot, K., Fehr, T., Saavedra, L., Leppelmeier, G. W., and Fraisse, R.: Global ozone monitoring by occultation of stars: an overview of GOMOS measurements on ENVISAT, *Atmos. Chem. Phys.*, 10, 12091-12148, doi:10.5194/acp-10-12091-2010, 2010.
- Bourassa, A. E., Degenstein, D. A., Elash, B. J., and Llewellyn, E. J.: Evolution of the stratospheric aerosol enhancement following the eruptions of Okmok and Kasatochi: OdinOSIRIS measurements, *J. Geophys. Res.*, 115, D00L03, doi:10.1029/2009jd013274, 2010.
- Bourassa, A. E., Rieger, L. A., Lloyd, N. D., and Degenstein, D. A.: Odin-OSIRIS stratospheric aerosol data product and SAGE III intercomparison, *Atmos. Chem. Phys.*, 12, 605-614, doi:10.5194/acp-12-605-2012, 2012.
- Bourassa, A. E., Robock, A., Randel, W. J., Deshler, T., Rieger, L. A., Lloyd, N. D., Llewellyn, E. J., and Degenstein, D. A.: Large Volcanic Aerosol Load in the Stratosphere Linked to Asian Monsoon Transport, 2012, *Science*, 337, 78-81, 2012.
- Brock, C. A., Hamill, P., Wilson, J. C., Jonsson, H. H., and Chan, K. R.: Particle Formation in the Upper Tropical Troposphere – a Source of Nuclei for the Stratospheric Aerosol, *Science*, 270, 1650-1653, 1995.
- Carn, S. A., Yang, K., Prata, A. J. and Krotkov, N. A.: Extending the long-term record of volcanic SO₂ emissions with the Ozone Mapping and Profiler Suite nadir mapper, *Geophys. Res. Lett.*, 42, 925-932, doi:10.1002/2014GL062437, 2015.
- DeLand, M., Bhartia, P. K., Xu, P. and Zhu, T.: OMPS Limb Profiler Aerosol Extinction Product AER675: Version 0.5 Data Release Notes, https://ozoneaq.gsfc.nasa.gov/media/docs/OMPS_LP_AER675_V0.5_Release_Notes.pdf, 2016.
- Deshler, T., Anderson-Sprecher, R., Jager, H., Barnes, J., Hofmann, D. J., Clemesha, B., Simonich, D., Osborn, M., Grainger, R. G., and Godin-Beekmann, S.: Trends in the nonvolcanic component of stratospheric aerosol over the period 1971 - 2004, *J. Geophys. Res.*, 111, D01201, doi:10.1029/2005JD006089, 2006.
- Deshler, T.: A review of global stratospheric aerosol: Measurements, importance, life cycle, and stratospheric aerosol, *Atmos. Res.*, 90, 223-232, 2008.
- Chazette, P., David, C., Lefrere, J., Godin, S., Pelon, J., and Megie, G.: Comparative lidar study of the optical, geometrical, and dynamical properties of stratospheric post-volcanic aerosols, following the eruption of El Chichon and Mount Pinatubo, *J. Geophys. Res.*, 100, 23 195-23 207, 1995.



- Godin-Beekmann, S., Porteneuve, J., Garnier, A.: Systematic DIAL lidar monitoring of the stratospheric ozone vertical distribution at observatoire de haute-provence (43.92 N, 5.71 E). *Journal of environmental Monitoring*, 5(1), 57-67, 2003.
- 625 Goldfarb, L., Keckhut, P., Chanin, M.-L., and Hauchecorne, A.: Cirrus climatological results from lidar measurements at OHP (44° N, 6° E), *Geophys. Res. Lett.*, 28, 1687–1690, 2001.
- Fairlie, T. D., Vernier, J.-P., Natarajan, M., and Bedka, K. M.: Dispersion of the Nabro volcanic plume and its relation to the Asian summer monsoon, *Atmos. Chem. Phys.*, 14, 7045-7057, 630 doi:10.5194/acp-14-7045-2014, 2014.
- Fernald, F. G.: Analysis of atmospheric lidar observations: some comments, *Appl. Opt.*, 23, 652–653, 1984.
- Fiocco, G. and Grams, G.: Observations of the Aerosol Layer at 20 km by Optical Radar, *J. Atmos. Sci.*, 21, 323–324, 1964.
- 635 Fromm, M., Shettle, E. P., Fricke, K. H., Ritter, C., Trickl, T., Giehl, H., Gerding, M., Barnes, J., O'Neill, M., Massie, S. T., Blum, U., McDermid, I. S., Leblanc, T., and Deshler, T.: The stratospheric impact of the Chisholm PyroCumulonimbus eruption: 2. Vertical profile perspective, *J. Geophys. Res.*, 113, D08203, doi:10.1029/2007JD009147, 2008.
- Fromm, M., Lindsey, D. T., Servranckx, R., Yue, G., Trickl, T., Sica, R., Doucet, P., and 640 Godin-Beekmann, S.: The Untold Story of Pyrocumulonimbus, *B. Am. Meteorol. Soc.*, 91, 1193–1209, 2010.
- Fyfe, J. C., von Salzen, K., Cole, J. N. S., Gillett, N. P., and Vernier, J.-P.: Surface response to stratospheric aerosol changes in a coupled atmosphere–ocean model, *Geophys. Res. Lett.*, 40, 584–588, doi:10.1002/grl.50156, 2013.
- 645 Garny, H. and Randel, W. J.: Transport pathways from the Asian monsoon anticyclone to the stratosphere, *Atmos. Chem. Phys.*, 16, 2703-2718, doi:10.5194/acp-16-2703-2016, 2016.
- Hauchecorne, A., Chanin, M.-L., Keckhut, P., and Nedeljkovic, D.: Lidar monitoring of the temperature in the middle and lower atmosphere, *App. Phys. B*, 55, 29–34, 1992.
- Haywood, J. M., Jones, A., Clarisse, L., Bourassa, A., Barnes, J., Telford, P., Bellouin, N., 650 Boucher, O., Agnew, P., Clerbaux, C., Coheur, P., Degenstein, D., and Braesicke, P.: Observations of the eruption of the Sarychev volcano and simulations using the HadGEM2 climate model, *J. Geophys. Res.*, 115, D21212, doi:10.1029/2010JD014447, 2010.
- Hitchman, M. H., McKay, M., and Trepte, C. R.: A climatology of stratospheric aerosol, *J. Geophys. Res.*, 99, 20689–20700, 1994.
- 655 Hofmann, D., Barnes, J., O'Neill, M., Trudeau, M., and Neely, R.: Increase in background stratospheric aerosol observed with lidar at Mauna Loa Observatory and Boulder, Colorado, *Geophys. Res. Lett.*, 36, L15808, doi:10.1029/2009GL039008, 2009.
- Holton, J. R., Haynes, P. H., McIntyre, M. E., Douglass, A. R., Rood, R. B., and Pfister, L.: Stratosphere-Troposphere Exchange, *Rev. Geophys.*, 33, 403–439, 1995.
- 660 Hoor, P., Wernli, H., Hegglin, M. I., and Bönisch, H.: Transport timescales and tracer properties in the extratropical UTLS, *Atmos. Chem. Phys.*, 10, 7929-7944, doi:10.5194/acp-10-7929-2010, 2010.
- Jaross, G., P. K. Bhartia, G. Chen, M. Kowitt, M. Haken, Z. Chen, P. Xu, J. Warner, and T. 665 Kelly: OMPS Limb Profiler instrument performance assessment, *J. Geophys. Res. Atmos.*, 119, 421 doi:10.1002/2013JD020482, 2014.
- Jäger, H.: Long-term record of lidar observations of the stratospheric aerosol layer at Garmisch-Partenkirchen, *J. Geophys. Res.*, 110, D08106, doi:10.1029/2004JD005506, 2005.
- Jäger, H. and Deshler, T.: Lidar backscatter to extinction, mass and area conversions for stratospheric aerosols based on midlatitude balloon-borne size distribution measurements, *Geophys. Res. Lett.*, 29, 1929, doi:10.1029/2002GL015609, 2002.
- 670 Jäger, H. and Deshler, T.: Correction to “Lidar backscatter to extinction, mass and area conversions for stratospheric aerosols based on midlatitude balloonborne size distribution measurements”, *Geophys. Res. Lett.*, 30, 1382, doi:10.1029/2003GL017189, 2003.



- 675 Junge, C. E., Chagnon, C. W., and Manson, J. E.: A Worldwide Stratospheric Aerosol Layer, *Science*, 133, 1478–1479, doi:10.1126/science.133.3463.1478-a, 1961.
- Keckhut, P., Hauchecorne, A., Bekki, S., Colette, A., David, C., and Jumelet, J.: Indications of thin cirrus clouds in the stratosphere at mid-latitudes, *Atmos. Chem. Phys.*, 5, 3407–3414, doi:10.5194/acp-5-3407-2005, 2005.
- 680 Klett, J. D.: Lidar inversion with variable backscatter/extinction ratios, *Appl. Opt.*, 24, 1638–1643, 1985.
- Kremser, S., et al.: Stratospheric aerosol - Observations, processes, and impact on climate, *Rev. Geophys.*, 54, doi:10.1002/2015RG000511, 2016.
- 685 Kristiansen, N. I., Prata, A. J., Stohl, A., and Carn, S. A.: Stratospheric volcanic ash emissions from the 13 February 2014 Kelut eruption, *Geophys. Res. Lett.*, 42, 588–596, doi:10.1002/2014GL062307, 2015.
- Lawrence, M. G., and Lelieveld, J.: Atmospheric pollutant outflow from southern Asia: A review, *Atmos. Chem. Phys.*, 10, 11,017–11,096, doi:10.5194/acp-10-11017-2010, 2010.
- Lefrere, J., Pelon, J., Cahen, C., Hauchecorne, A., and Flamant, P.: Lidar survey of the post Mt. St. Helens stratospheric aerosol at Haute Provence Observatory, *Appl. Opt.* 20, A70–1117, 1981.
- 690 Livesey, N. J., Read, W. G., Wagner, P. A., Froidevaux, L., Lambert, A., Manney, G. L., Millán-Valle, L. F., Pumphrey, H. C., Santee, M. L., Schwartz, M. J., Wang, S., Fuller, R. A., Jarnot, R. F., Knosp, B. W., and Martinez, E.: Version 4.2x Level 2 data quality and description document, Tech. Rep. JPL D-33509, NASA Jet Propulsion Laboratory, version 4.2x-1.0, 2015.
- McLinden, C., et al.: OSIRIS: A decade of scattered light, *Bull. Am. Meteorol. Soc.*, 93(12), 695 1845–1863, 2012.
- Mills, M. J., Schmidt, A., Easter, R., Solomon, S., Kinnison, D. E., Ghan, S. J., Neely, R. R. III, Marsh, D. R., Conley, A., Bardeen, C. G. et al.: Global volcanic aerosol properties derived from emissions, 1990–2014, using CESM1(WACCM), *J. Geophys. Res. Atmos.*, 121, 2332–2348, doi:10.1002/2015JD024290, 2016.
- 700 Mote, P., Rosenlof, K. H., Holton, J. R., Harwood, R. S., and Waters, J. W.: An atmospheric tape recorder: The imprint of tropical tropopause temperatures on stratospheric water vapor, *J. Geophys. Res.*, 101, 3989–4006, 1996.
- Müller, S., Hoor, P., Bozem, H., Gute, E., Vogel, B., Zahn, A., Bönisch, H., Keber, T., Krämer, M., Rolf, C., Riese, M., Schlager, H., and Engel, A.: Impact of the Asian monsoon on the 705 extratropical lower stratosphere: trace gas observations during TACTS over Europe 2012, *Atmos. Chem. Phys.*, 16, 10573–10589, doi:10.5194/acp-16-10573-2016, 2016.
- Neely, R. R., III et al.: Recent anthropogenic increases in SO₂ from Asia have minimal impact on stratospheric aerosol, *Geophys. Res. Lett.*, 40, 999–1004, doi:10.1002/grl.50263, 2013.
- 710 Park, M., Randel, W. J., Gettelman, A., Massie, S. T., and Jiang, J. H.: Transport above the Asian summer monsoon anticyclone inferred from Aura Microwave Limb Sounder tracers, *J. Geophys. Res.*, 112, D16309, doi:10.1029/2006JD008294, 2007.
- Prata, A. J., Carn, S. A., Stohl, A., and Kerkmann, J.: Long range transport and fate of a stratospheric volcanic cloud from Soufrière Hills volcano, Montserrat, *Atmos. Chem. Phys.*, 7, 5093–5103, doi:10.5194/acp-7-5093-2007, 2007.
- 715 Randel, W. J., Park, M., Emmons, L., Kinnison, D., Bernath, P., Walker, K. A., Boone, C., and Pumphrey, H.: Asian monsoon transport of pollution to the stratosphere, *Science*, 328, 611–613, doi:10.1126/science.1182274, 2010.
- Ridley, D. A., Solomon, S., Barnes, J. E., Burlakov, V. D., Deshler, T., Dolgii, S. I., Herber, A. B., Nagai, T., Neely, R. R., Nevzorov, A. V., Ritter, C., Sakai, T., Santer, B. D., Sato, M., Schmidt, 720 A., Uchino, O., and Vernier, J. P.: Total volcanic stratospheric aerosol optical depths and implications for global climate change, *Geophys. Res. Lett.*, 41, 7763–7769, doi:10.1002/2014GL061541, 2014.
- Romero, J. E., et al.: Eruption dynamics of the 22–23 April 2015 Calbuco volcano (southern Chile): Analyses of tephra fall deposits, *J. Volcanol. Geotherm. Res.*, 317, 15–29, 2016.



- Russell, P. B., and McCormick, M. P.: SAGE II aerosol data validation and initial data use: An introduction and overview, *J. Geophys. Res.*, 94(D6), 8335–8338, doi:10.1029/JD094iD06p08335, 1989.
- 730 Sakai, T., Uchino, O., Nagai, N., Liley, B., Morino, I. and Fujimoto, T.: Long-term variation of stratospheric aerosols observed with lidars over Tsukuba, Japan, from 1982 and Lauder, New Zealand, from 1992 to 2015, *J. Geophys. Res. Atmos.*, 121, doi:10.1002/2016JD025132, 2016.
- 735 Santer, B. D., Bonfils, C., Painter, J. F., Zelinka, M. D., Mears, C., Solomon, S., Schmidt, G. A., Fyfe, J. C., Cole, J. N. S., Nazarenko, L., Taylor, K. E., and Wentz, F. J.: Volcanic contribution to decadal changes in tropospheric temperature, *Nat. Geosci.*, 7, 185–189, doi:10.1038/ngeo2098, 2014.
- Santer, B. D., et al.: Observed multivariable signals of late 20th and early 21st century volcanic activity, *Geophys. Res. Lett.*, 42, 500–509, doi:10.1002/2014GL062366, 2015.
- 740 Schwartz, M. J., Manney, G. L., Hegglin, M. I., Livesey, N. J., Santee, M. L., and Daffer, W. H.: Climatology and variability of trace gases in extratropical double-tropopause regions from MLS, HIRDLS and ACE-FTS measurements, *J. Geophys. Res.*, 120, 843–867, doi:10.1002/2014JD021964, 2015.
- 745 Smith, S. J., van Aardenne, J., Klimont, Z., Andres, R. J., Volke, A., and Delgado Arias, S.: Anthropogenic sulfur dioxide emissions: 1850–2005, *Atmos. Chem. Phys.*, 11, 1101–1116, doi:10.5194/acp-11-1101-2011, 2011.
- Solomon, S., Daniel, J. S., Neely, R. R., Vernier, J.-P., Dutton, E. G., and Thomason, L. W.: The Persistently Variable “Background” Stratospheric Aerosol Layer and Global Climate Change, *Science*, 333, 866–870, doi:10.1126/science.1206027, 2011.
- 750 SPARC/ASAP: WMO/SPARC Scientific Assessment of Stratospheric Aerosol Properties (ASAP), WCRP-124 WMO/TD- No. 1295, SPARC Report No. 4, edited by: Thomason, L. and Peter, Th., WMO, 2006.
- Thomason, L. W., Burton, S. P., Luo, B.-P., and Peter, T.: SAGE II measurements of stratospheric aerosol properties at non-volcanic levels, *Atmos. Chem. Phys.*, 8, 983–995, doi:10.5194/acp-8-983-2008, 2008.
- 755 Thomason, L. W. and Vernier, J.-P.: Improved SAGE II cloud/aerosol categorization and observations of the Asian tropopause aerosol layer: 1989–2005, *Atmos. Chem. Phys.*, 13, 4605–4616, doi:10.5194/acp-13-4605-2013, 2013.
- 760 Trepte, C. R. and Hitchman, M. H.: Tropical stratospheric circulation deduced from satellite aerosol data, *Nature*, 355, 626–628, 1992.
- Trickl, T., Giehl, H., Jäger, H., and Vogelmann, H.: 35 yr of stratospheric aerosol measurements at Garmisch-Partenkirchen: from Fuego to Eyjafjallajökull, and beyond, *Atmos. Chem. Phys.*, 13, 5205–5225, doi:10.5194/acp-13-5205-2013, 2013.
- 765 Vanhellefont, F., Fussen, D., Matshvili, N., Tétard, C., Bingen, C., Dekemper, E., Loodts, N., Kyrölä, E., Sofieva, V., Tamminen, J., Hauchecorne, A., Bertaux, J.-L., Dalaudier, F., Blanot, L., Fanton d'Andon, O., Barrot, G., Guirlet, M., Fehr, T., and Saavedra, L.: Optical extinction by upper tropospheric/stratospheric aerosols and clouds: GOMOS observations for the period 2002–2008, *Atmos. Chem. Phys.*, 10, 7997–8009, doi:10.5194/acp-10-7997-2010, 2010.
- 770 Vanhellefont, F., Matshvili, N., Blanot, L., Robert, C. É., Bingen, C., Sofieva, V., Dalaudier, F., Tétard, C., Fussen, D., Dekemper, E., Kyrölä, E., Laine, M., Tamminen, J., and Zehner, C.: AerGOM, an improved algorithm for stratospheric aerosol extinction retrieval from GOMOS observations – Part 1: Algorithm description, *Atmos. Meas. Tech.*, 9, 4687–4700, doi:10.5194/amt-9-4687-2016, 2016.
- 775 Vogel, B., Günther, G., Müller, R., Groß, J.-U., Hoor, P., Krämer, M., Müller, S., Zahn, A., and Riese, M.: Fast transport from Southeast Asia boundary layer sources to northern Europe: rapid uplift in typhoons and eastward eddy shedding of the Asian monsoon anticyclone, *Atmos. Chem. Phys.*, 14, 12745–12762, doi:10.5194/acp-14-12745-2014, 2014.
- Vernier, J. P., Pommereau, J. P., Garnier, A., Pelon, J., Larsen, N., Nielsen, J., Christensen, T., Cairo, F., Thomason, L. W., Leblanc, T., and McDermid, I. S.: The tropical stratospheric aerosol



780 layer from CALIPSO lidar observations, *J. Geophys. Res.*, 114, D00H10,
doi:10.1029/2009JD011946, 2009.

Vernier, J. P., Thomason, L. W., Pommereau, J. P., Bourassa, A., Pelon, J., Garnier, A.,
Hauchecorne, A., Blanot, L., Trepte, C., Degenstein, D., and Vargas, F.: Major influence of tropical
volcanic eruptions on the stratospheric aerosol layer during the last decade, *Geophys. Res. Lett.*, 38,
785 L12807, doi:10.1029/2011GL047563, 2011a.

Vernier, J.-P., Thomason, L. W., and Kar, J.: CALIPSO detection of an Asian tropopause
aerosol layer, *Geophys. Res. Lett.*, 38, L07804, doi:10.1029/2010GL046614, 2011b.

Vernier, J.-P., Pommereau, J.-P., Thomason, L. W., Pelon, J., Garnier, A., Deshler, T., Jumelet,
J., and Nielsen, J. K.: Overshooting of clean tropospheric air in the tropical lower stratosphere as
790 seen by the CALIPSO lidar, *Atmos. Chem. Phys.*, 11, 9683-9696, doi:10.5194/acp-11-9683-2011,
2011c.

Vernier, J.-P., Thomason, L., Fairlie, T. D., Minnis, P., Palikonda, R., and Bedka, K. M.:
Comment on “Large volcanic aerosol load in the stratosphere linked to Asian monsoon transport”,
Science, 339, 6120, doi:10.1126/science.1227817, 2013

795 Vernier, J. P., Fairlie, T. D., Natarajan, M., Wienhold, F. G., Bian, J., Martinsson, B. G.,
Crumevolle, S., Thomason, L. W., and Bedka, K. M.: Increase in upper tropospheric and lower
stratospheric aerosol levels and its potential connection with Asian pollution, *J. Geophys. Res.-
Atmos.*, 120, 1608–1619, doi:10.1002/2014JD022372, 2015.

800 Waters, J. W., L. Froidevaux, R.S. Harwood, R.F. Jarnot, H.M. Pickett, W.G. Read, J.R.
Holden: The earth observing system microwave limb sounder (EOS MLS) on the Aura
satellite. *Geoscience and Remote Sensing, IEEE Transactions on*, 44(5), 1075-1092, 2006.

Winker, D. M., Pelon, J., Coakley Jr., J. A., Ackerman, S. A., Charlson, R. J., Colarco, P. R.,
Flamant, P., Fu, Q., Hoff, R., Kittaka, C., Kubar, T. L., LeTreut, H., McCormick, M. P., Megie, G.,
Poole, L., Powell, K., Trepte, C., Vaughan, M. A., and Wielicki, B. A.: The CALIPSO Mission: A
805 Global 3D View Of Aerosols And Clouds, *Bull. Amer. Meteor. Soc.*, 91, 1211–1229,
doi:10.1175/2010BAMS3009.1, 2010.

Yu, P., Toon, O. B., Neely, R. R., Martinsson, B. G., and Brenninkmeijer, C. A. M.:
Composition and Physical Properties of the Asian Tropopause Aerosol Layer and the North
American Tropospheric Aerosol Layer, *Geophys. Res. Lett.*, 42(7), doi:10.1002/2015GL063181,
810 2015.

815

820

825

830



835

$\Delta_{\text{mean}} \pm 2\text{SE}, \%$	LiO3S	LTA	SAGE II	GOMOS	OSIRIS	CALIOP	OMPS	Sat mean
LiO3S		0.65 ± 2.4	2.1 ± 3.3	0.4 ± 4.0	-6.6 ± 3.4	-2.9 ± 3.2	-4.8 ± 4.3	-1.5 ± 2.2
LTA			-2.1 ± 4.4	-2.9 ± 4.3	-7.4 ± 2.7	-0.4 ± 2.5	-8.6 ± 3.3	-2.7 ± 2.1
SAGE II				-0.1 ± 5.9	7.7 ± 6.0	-	-	2.1 ± 2.7
GOMOS					-5.8 ± 3.4	-1.6 ± 3.7	-	-1.9 ± 1.9
OSIRIS						7.7 ± 2.1	6.6 ± 4.0	3.2 ± 1.3
CALIOP							-5.5 ± 2.7	-3.1 ± 1.2

R correl	LiO3S	LTA	SAGE II	GOMOS	OSIRIS	CALIOP	OMPS	Sat mean
LiO3S		0.9	0.97	0.9	0.81	0.85	0.63	0.94
LTA			0.96	0.86	0.9	0.93	0.66	0.94
SAGE II				0.7	0.85	-	-	
GOMOS					0.86	0.88	-	
OSIRIS						0.93	0.65	
CALIOP							0.71	

840 **Table 1.** Intercomparison of stratospheric Aerosol Optical Depth between 17 and 30 km (sAOD₁₇₃₀) series displayed in Fig. 1. Mean relative difference $\Delta_{\text{mean}} \pm 2$ standard errors (top) and correlation coefficient R (bottom).

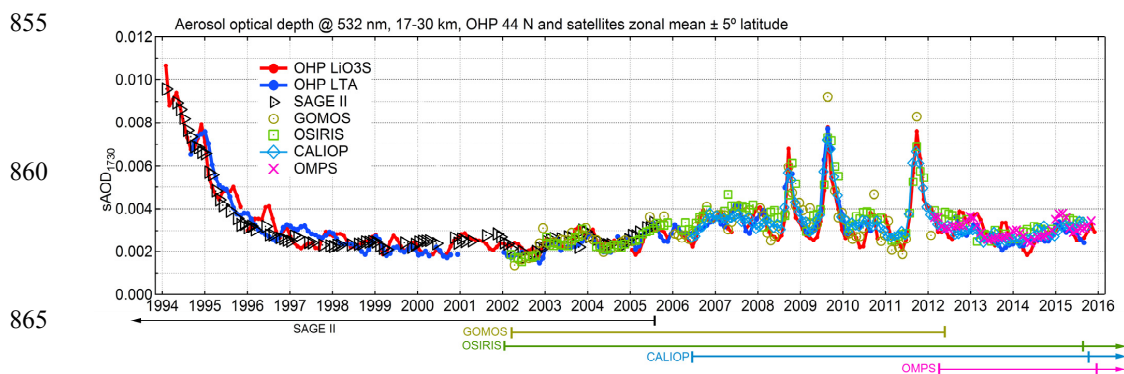
Volcano (VEI =4)	Eruption date	Latitude	Start of period	End of period
Rabaul (Ra)	September 1994	4°S	October 1994	Undefined
Ulawun (Ul)	September 2000	5°S	Undetected	Undetected
Shiveluch (Sh)	May 2001	56°N	Undetected	Undetected
Ruang (Ru)	September 2002	2°N	November 2003	February 2004
Reventador (Re)	November 2002	0°N	November 2003	February 2004
Manam (Ma)	January 2005	4°S	April 2005	February 2006
Soufrière Hills (So)	May 2006	16°N	August 2006	Undefined
Tavurvur (Ta)	October 2006	4°S	Undefined	February 2008
Okmok (Ok)	July 2008	55°N	August 2008	January 2009
Kasatochi (Ka)	August 2008	55°N	August 2008	January 2009
Sarychev (Sa)	June 2009	48°N	June 2009	December 2009
Merapi (Me)	October 2010	7°S	December 2010	February 2011
Nabro (Na)	June 2011	13°N	July 2011	February 2013
Kelud (Ke)	February 2014	8°S	January 2015	April 2015

845

Table 2. List of volcanic eruptions of Volcanic Explosivity Index VEI=4 occurring in the tropics and Northern hemisphere (>20°S) between 1994 and 2016 as reported by Smithsonian Institution Global Volcanism Program (<http://volcano.si.edu>). Temporal extent of the volcanically-perturbed period

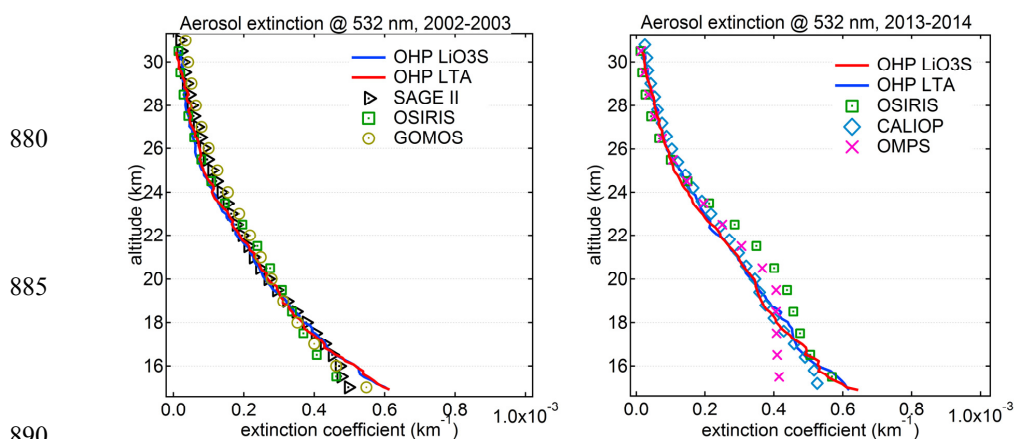


850 from the corresponding eruption is provided in the rightmost two columns (see Fig. 3 and text for
 855 detail).



865
 870 **Figure 1. Time series of monthly-mean $sAOD_{1730}$ from OHP lidars and monthly/zonal mean $sAOD_{1730}$ within 40° - 50° N from satellite sounders. Average statistical error of monthly-mean $sAOD_{1730}$ from OHP lidars is provided in the embedded panel as error bars (two standard errors) scaled to the principal vertical axis. Time spans and data availability of satellite missions are shown below the panel.**

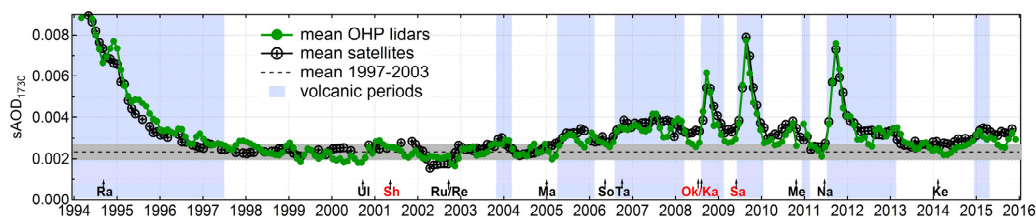
875



880
 885
 890 **Figure 2. Comparison of aerosol extinction profiles at 532 nm from OHP lidars and satellites averaged over volcanically-quietest periods 2002-2003 (left) and 2013-2014 (right).**

895

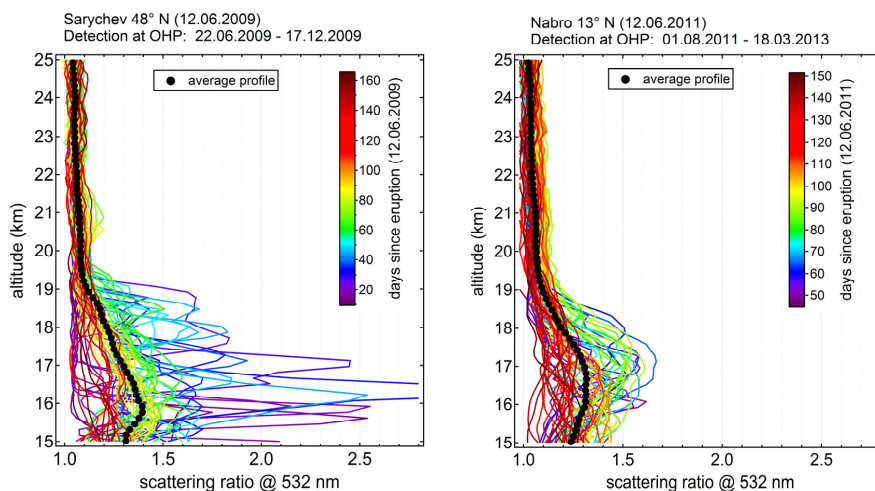
900



905 **Figure 3. Time series of monthly-mean $sAOD_{1730}$ computed by averaging both OHP lidars and all**
satellites. VEI 4 eruptions $>20^{\circ}S$ (Tab. 2) are indicated along the x-axis, NH mid-latitude eruptions are
marked in red. Time periods considered as perturbed by volcanism are shaded light blue. See text for
details.

910

915



920

925

930

935

Figure 4. Individual (coloured curves) and period-averaged (black circles) scattering ratio
profiles from OHP LiO3S lidar acquired after the eruptions of Sarychev (left) and Nabro
(right) volcanoes. The colours of individual profiles denote the days since eruption. The
eruption dates and plume detection periods are indicated in each panel.

940

945



950

955

960

965

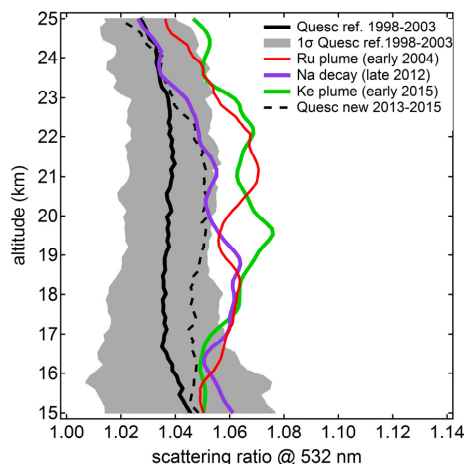
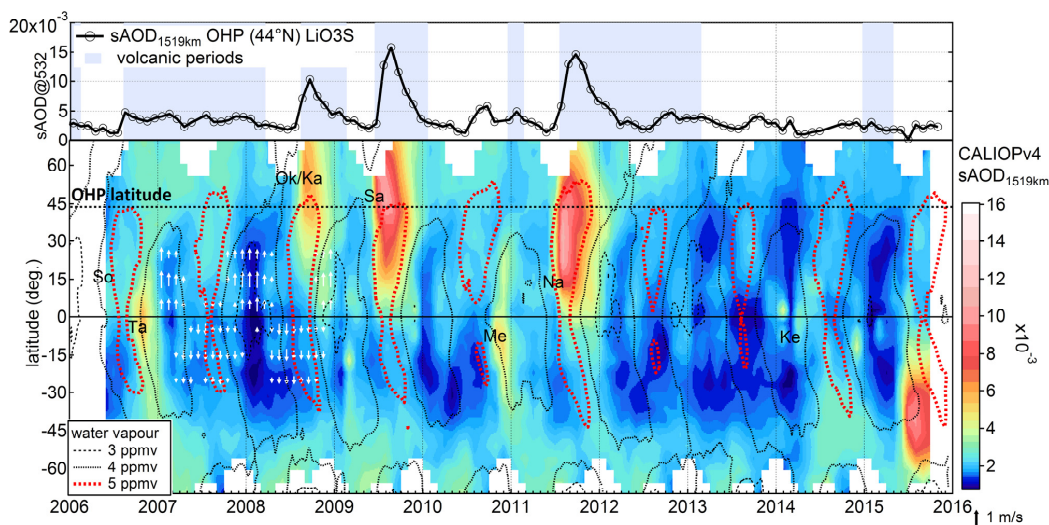


Figure 5. Vertical profiles of scattering ratio (532 nm) averaged over different periods: “reference” quiescent period (Quesc ref. 1997-2003) and its one standard deviation range (1σ Quesc. ref.); aged volcanic plumes of Ruang/Reventador (red), Nabro in late 2012 (violet); Kelud (green); post-Nabro quiescent period (Quesc new, black dashed). See Fig. 3 and Tab. 2 for detail on period definition.

970



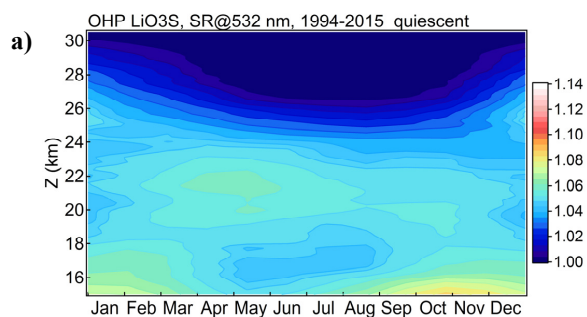
975

Figure 6. Time series of monthly-mean $sAOD_{1519}$ from OHP LiO3S lidar (top) and time-latitude section of $sAOD_{1519}$ from CALIOP in log-scaled color map with indications of VEI 4 eruptions (bottom). Time periods considered as perturbed by volcanism (Tab. 2) are shaded light blue in the top panel. White arrows (in 2007-2008) represent the mean meridional component of monthly/zonally-averaged horizontal wind at 100 hPa from ERA-Interim reanalysis. Dashed and dotted contours depict zonal-mean water vapour mixing ratio at 100 hPa from Aura MLS.

980



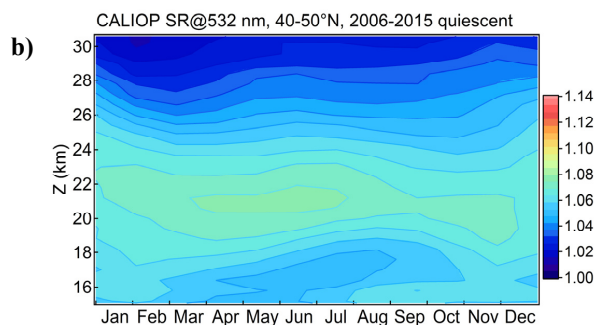
985



990

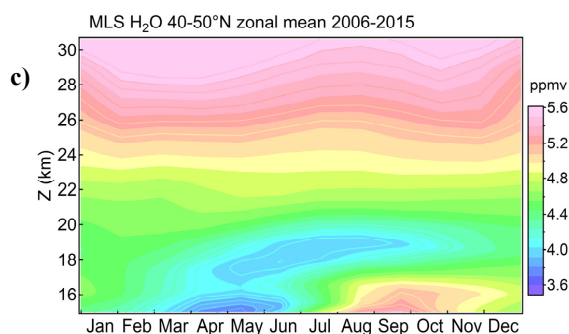
995

1000



1005

1010



1015

1020

1025

1030

Figure 7. Climatological month-altitude sections of a) SR from OHP LiO₃S lidar for selected volcanically-quiescent periods over the entire measurement time span (1994-2015); b) zonal-mean SR at 40°-50° N from CALIOP, June 2006 - September 2015 for selected volcanically-quiescent periods (Tab. 2); c) zonal mean water vapour at 40°-50° N from MLS, June 2006 - September 2015.

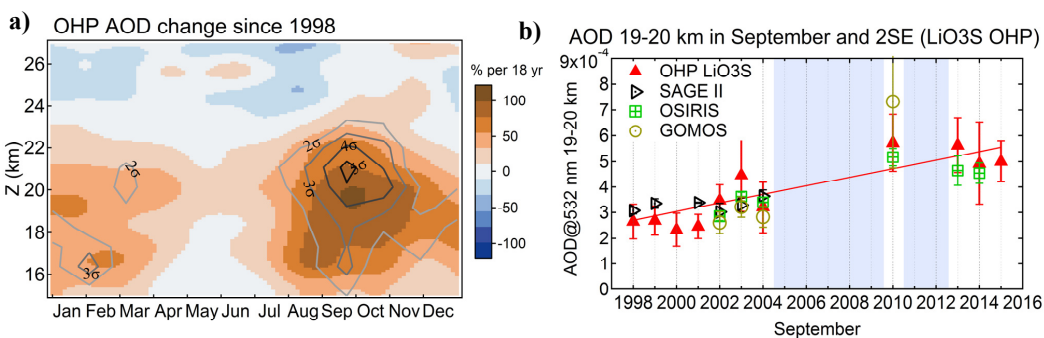


1035

1040

1045

1050



1055

Figure 8. (a) Monthly-averaged 1-km AOD change since 1998 from OHP LiO3S lidar based on the observations during volcanically-unperturbed periods. Statistically significant changes above 95% confidence interval are encircled by grey-scaled contours. (b) Evolution of the AOD in the 19-20 km layer in September from OHP LiO3S lidar and satellite observations above Western Mediterranean. Error bars denote two times the standard error. Shaded areas indicate the volcanically-perturbed periods.